Journal Pre-proof

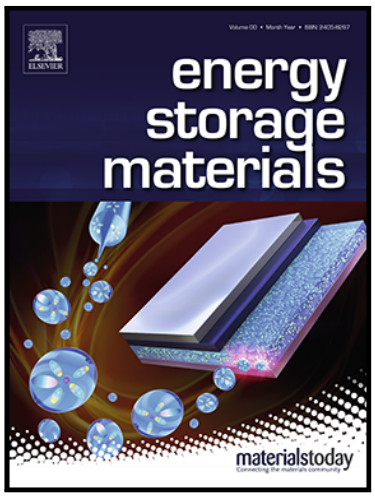

Using CrN_4 Moiety to Weaken the Dissociation Barrier of Hydroxyl on Adjacent Single Iron Atom for Efficient Oxygen Reduction

Lilian Wang , Li Yang , Xinyu Zhao , Hang Ma , Bohuai Pang , Lingyan Duan , Kun Zeng , Lu Liu , Anran Chen , Hong Guo

PII: S2405-8297(24)00753-0
DOI: https://doi.org/10.1016/j.ensm.2024.103927
Reference: ENSM 103927

To appear in: *Energy Storage Materials*

Received date: 2 October 2024
Revised date: 5 November 2024
Accepted date: 21 November 2024

Please cite this article as: Lilian Wang , Li Yang , Xinyu Zhao , Hang Ma , Bohuai Pang , Lingyan Duan , Kun Zeng , Lu Liu , Anran Chen , Hong Guo , Using CrN_4 Moiety to Weaken the Dissociation Barrier of Hydroxyl on Adjacent Single Iron Atom for Efficient Oxygen Reduction, *Energy Storage Materials* (2024), doi: https://doi.org/10.1016/j.ensm.2024.103927

Highlights

- ORR activity depends on orbital level before being further evaluated by bond order.
- Cr=N_2=Fe ABCs is developed using a time-/energy-saving Joule heating strategy (~ 10s).
- Higher ORR activity than commercial Pt/C and stable operation of ZAB for over 300 h.

Using CrN_4 Moiety to Weaken the Dissociation Barrier of Hydroxyl on Adjacent Single Iron Atom for Efficient Oxygen Reduction

Lilian Wang [a], Li Yang [a], Xinyu Zhao [a], Hang Ma [c], Bohuai Pang [a], Lingyan Duan [a], Kun Zeng [a], Lu Liu [a], Anran Chen [a,*], and Hong Guo [a,b,*]

[a] School of Materials and Energy, International Joint Research Center for Advanced Energy Materials of Yunnan Province, Yunnan Key Laboratory of Carbon Neutrality and Green Low-carbon Technologies, Yunnan University, Kunming 650091, China

[b] Southwest United Graduate School, Kunming 650091, China

[c] R & D Center, Yunnan Yuntianhua Co., Ltd., Kunming 650228, China

*Corresponding author: guohong@ynu.edu.cn (Hong Guo)

anran@ynu.edu.cn (Anran Chen)

Abstract: The strong perturbation of the valence band within the entire material system and accelerated $^*OH$ dissociation from Fe site are triggered by incorporating CrN_4 moiety with low Fenton effect and $^*OH$ adsorption energy. This atomically dispersed $Cr{=}N_2{=}Fe$ electrocatalyst is developed by adopting a super time-/energy-saving Joule heating strategy (~ 10s). Through the investigation of valence orbital energy levels and valence electron behavior for the prepared catalysts, in combination with in-situ Raman testing and theoretical calculations, we have determined that the interaction between the metal sites and oxygen-containing intermediates primarily depends on orbital energy levels before being further evaluated by bond order involving electronic modulation. This finding may offer a valuable insight for future research in related electrocatalysis fields. The $Cr{=}N_2{=}Fe$ catalyst exhibits higher ORR catalytic capability than commercial Pt/C, thus driving stable operation of the assembled zinc-air battery for over 300 h.

Keywords: Joule heating, valence band, in-situ spectroelectrochemistry, CrN_4 moiety, oxygen reduction

1. Introduction

Given the low turnover frequency, poor methanol tolerance and scarcity of commercial Pt/C as ORR catalysts for sustainable energy conversion zinc-air batteries,

there is a strong need to develop suitable alternatives.[1,2] The widely recommended candidates are single-atom catalysts (SACs), especially atomic-level bimetallic catalysts (ABCs).[3–8] However, most of the reported SACs preparation methods are energy-intensive long-term tubular furnace pyrolysis, which makes it impossible to achieve industrial production with economic considerations. More fatally, such long-term (~ hours) high temperature treatment may lead to metal atom agglomeration, resulting in low atom utilization efficiency and poor catalytic composition/structure. Joule heating technology can provide ultra-high temperature (up to 3000 K) and ultra-fast heating/cooling rates, often completing the entire pyrolysis process in seconds or tens of seconds.[9,10] This ultra-fast processing effectively suppresses metal agglomeration to produce highly dispersed metal active sites, greatly reduces pyrolysis losses to achieve a higher yield, and more importantly, exhibits a very low energy consumption. Based on current reports on the preparation of SACs using Joule heating, this method is considered to be a promising alternative to traditional process for preparing SACs[11–13].

Among the many SACs, extensive experimental evidence and theoretical calculations have demonstrated that FeN_4 moieties can be widely used as a favorable catalytic active center for ORR processes, as its unique *d*-band electronic structure allows for a certain degree of *d-p* orbital bonding with oxygen intermediates.[14] However, although FeN_4 is favorable for achieving the adsorption of O_2 and the cleavage of O=O, its unfavorable $^*OH$ desorption step has usually been an obstacle to the regeneration of the FeN_4 sites.[2,15,16] FeN_4 is also greatly affected by the Fenton effect, and there are serious oxidation corrosion problems.[17,18] Its durable stability can only be solved if the Fenton effect is decreased to a large extent. It is expected that a decrease in Fenton effect of FeN_4 may be achieved by coupling adjacent metal centers with less Fenton reaction inherently around it to further modulate the valence band structure of Fe site. Fortunately, CrN_4 moieties feature a very low activity in catalyzing Fenton reaction, which can lead to much higher stability than its FeN_4 counterpart.[19] CrN_4 also exhibits a low adsorption energy for $^*OH$, which may stimulate the desorption of $^*OH$ on the coupled adjacent FeN_4 sites.[20,21] Therefore, CrN_4 may be used as a high-quality candidate for coupling with FeN_4. At present, the potential of CrN_4 in oxygen electrocatalysis has been far from being appreciated. Another point worth mentioning is that studying the bonding behavior between metal sites and $^*OH$ is very important, as the release of $^*OH$ is generally the rate-determining step for Fe-based

catalysts.[15,22–24] However, the current researches in this area are still limited, and most reports almost only utilize orbital energy levels or bond orders to measure the interaction strength between active sites and oxygen species independently,[16,25] lacking more rigorous reports that link the two to jointly reveal the bonding behavior. The in-depth study of bonding behavior, the advance of CrN_4 research, and the use of Joule heating technology are the most significant differences between this work and previous reports on Fe-N-C modified by another metal atom.[26]

Inspired by the low Fenton effect and low adsorption energy for $^*OH$ of CrN_4 moieties, we designed a $Cr{=}N_2{=}Fe$ ABCs to weaken the Fenton reactivity of the material system while accelerating the desorption of $^*OH$ on Fe sites, thereby improving the intrinsic catalytic activity of FeN_4. The catalysts were synthesized using the super time-/energy-saving Joule heating method. Through careful study of the 3*d* valence orbital energy level and valence electron behavior for the synthesized catalyst, combined with in-situ spectroscopy and theoretical calculations, we acquire that the decrease of $^*OH$ dissociation barrier on Fe sites is mainly attributed to the following two aspects: (1) the addition of heterometals increases the pairing hardness between the donor and the acceptor during ORR process, as well as Fe-$^*OH$ antibonding orbital occupancy; (2) the introduction of CrN_4 moieties with strong affinity to $^*OH$ significantly increases the bond length of Fe-$^*OH$ and weakens the bond energy between them. It can be predicted that the prepared $Cr{=}N_2{=}Fe$ ABCs will exhibit an excellent oxygen reduction performance.

2. Experimental section

2.1. Chemicals

Nafion solution (5 wt%) and carbon black were produced by Sigma-Aldrich. Potassium hydroxide (KOH, ≥90%), chromic acetate ($C_6H_9O_6Cr$, 99%), iron(II) acetate ($C_4H_6O_4Fe$, 95%), and 1,10-phenanthroline monohydrate ($C_{12}H_{10}N_2O$, >99%) were purchased from the Tansoole platform. The commercial Pt/C (20 wt%), and RuO_2 (99.95%) were purchased from Aladdin. All chemicals were used without further purification unless otherwise stated.

2.2 Electrocatalyst synthesis

2.2.1. Synthesis of $Cr{=}N_2{=}Fe$ ABCs

Preparation of the precursor: 4.4 mg of iron(II) acetate, 17.2 mg of chromic acetate, and 69.4 mg of 1,10-phenanthroline monohydrate were dissolved in 30 mL ethanol to

form solution A. Simultaneously, 120 mg of carbon black (Ketjen black) were ultrasonic dispersed in 20 mL ethanol to form solution B. Subsequently, solution A was added dropwise into solution B under magnetic stirring. After incubating the mixed solution at room temperature for 30 min, it was separated by centrifugation and washed with ethanol several times, and finally vacuum dried overnight at 60 ℃ to obtain the carbon black precursor modified by metal-ligand complexes.

Pyrolysis of the precursor: The obtained precursor was placed into a graphite boat and transferred to a Joule furnace where it underwent Joule heat treatment in an Ar stream using a programmed mode with a current set at 305A. The monitoring window on the Joule device showed that the applied current induced rapid heating to reach a temperature of 1300 ℃ within three seconds, and then rapidly cooled to room temperature. This entire process took approximately ten seconds to complete. The resulting samples were named Cr=N_2=Fe ABCs.

2.2.2. Synthesis of other control samples

The atomic-level monometallic Fe catalysts (Fe AMCs) and Cr catalysts (Cr AMCs) were prepared using the same process as Cr=N_2=Fe ABCs, except that iron(II) acetate and chromic acetate was used only as the metal source. The preparation processes of nonmetallic catalysts (NMCs) were similar to the above-mentioned preparation processes, but no metal source was used.

Detailed information about material characterization, electrochemical measurements, Zn-air battery measurements, in-situ Raman and ATR-FTIR spectra measurements, and density functional theory (DFT) calculations can be found in the **Supporting Information**.

3. Results and discussion

3.1. Design principle of catalyst

DFT calculations were first implemented to acquire the Gibbs free energy of the 4e-ORR pathway in the designed catalyst models (Figures 1A and S1). The free energy diagram establishes that the rate-determining step (RDS) of Fe AMCs is *OH desorption. If we can screen out a different heterometallic ion with stronger *OH adsorption but with weak Fenton reaction and less oxidation corrosion as the synergistic site of Fe, it may significantly enhance the *OH desorption on FeN_4, thereby facilitating the regeneration of Fe active sites. To this end, we calculated the bond order of orbital interaction between several transition metal ions (common valence states) with ORR

potential and intermediate *OH in RDS (Figure 1B). The *d*-orbitals of metal ions simultaneously satisfies the following electron filling principles: (1) the lowest energy principle, (2) Pauli incompatibility principle, and (3) Hund rule. The increase in the number of 3*d* electrons will increase the antibonding orbital filling, thereby decreasing the bond order (Figure 1C). It is found that Cr ion exhibits the largest bond order to *OH, indicating the strongest adsorption. Therefore, selecting Cr ion as the ORR co-catalytic site of FeN_4 is very reasonable and ideal. As shown in Figure 1A, after the introduction of CrN_4 moieties in FeN_4, a significant reduction in the RDS barrier on Fe sites can be observed. During the ORR process of Cr=N_2=Fe ABCs, O_2 preferentially combines with the Fe center with a lower adsorption barrier in the first step, and then forms Fe-*OOH through single proton electron transfer (Figure S2). This may be related to the medium-spin Fe sites in Cr=N_2=Fe ABCs with a single d_z^2 electron to easily penetrate the antibonding π^*-orbital of O_2.[27,28] The corresponding Cr sites have no electrons in the d_z^2 orbital, making the Cr sites inactive for the initial ORR step. Finally, benefit from this short-range interaction between FeN_4 and CrN_4, the Fe-*OH bonds formed become longer under the influence of the Cr sites (strong *OH-philicity) (Figure 1D). This interaction between Cr and HO*-Fe should be due to the intermolecular van der Waals forces or hydrogen bonds, which causes the local electrons around Fe-O to be critically biased towards O, thus obviously reducing the dissociation barrier on Fe-*OH.[29] Further crystal orbital Hamilton population (COHP) analysis was conducted to study the bonding properties between the metal sites and *OH. As displayed in Figures 1E, S3 and S4, the integral COHP (ICOHP) values of Cr=N_2=Fe ABCs (Fe site: -2.71) and Cr=N_2=Fe ABCs (Cr site: -3.91) are both larger than those of Fe AMCs (-3.09) and Cr AMCs (-4.08), respectively, revealing less antibonding unoccupancy for Cr=N_2=Fe ABCs. The above theoretical calculation results demonstrate the rationality of our designed structure.

3.2. Study on microstructure and valence orbitals

The Cr=N_2=Fe ABCs and other control samples were prepared using the ultra-time-saving and energy-efficient Joule heating technique. As shown in Figures 1F and S5, the samples were induced rapid heating to reach a temperature of 1300 ℃ within three seconds by applying a 305 A of current. This whole preparation process takes approximately ten seconds to complete, which facilitates the optimization of the active structure of the products.[30] To confirm the successful synthesis of carbon-loaded

SACs, the structural properties of the obtained catalysts were investigated. In the X-ray diffraction (XRD) pattern of all prepared samples (Figure S6), no significant crystal peaks of metals/metal oxides are found, except for two peaks at 24° and 44° corresponding to the (002) and (100) facets of graphite.[2] The scanning transmission electron microscopy (STEM) pattern of all prepared samples shows that the structure of carbon black is well preserved after Joule heating without obvious signs of destruction (Figures S7-S9). The corresponding HAADF-STEM-energy dispersive X-ray spectroscopy (EDS) exhibits the uniform distribution of Fe, Cr, N and C elements throughout the carbon substrate. The Cr=N_2=Fe ABCs were further characterized by an aberration-corrected high angle annular dark field scanning transmission electron microscopy (AC-HAADF-STEM), and a number of evenly distributed bright dual-spot pairs caused by the elements Fe and Cr with high Z contrast are observed, providing evidence of atomic dispersion of the metal species (Figure 2A).[6] The coexistence of Fe and Cr elements in the Cr=N_2=Fe ABCs is further confirmed by the electron energy loss spectrum (EELS) (Figure 2B).[6] The intensity distribution of the adjacent two atoms exhibits different contrasts (left side of Figure 2C), also confirming that the atomic pairs are composed of two different elements. The distance between the atomic pairs is 2.5 Å (Figure 2C, D), which is consistent with the theoretical simulation model (right side of Figure 2C).[2,16,27,31,32] To validate the aforementioned structure, X-ray absorption fine structure (XAFS) measurements were performed. As depicted by the extended XAFS (EXAFS) in Figures 2E and 2F, Cr=N_2=Fe ABCs exclusively exhibits a prominent Fe-N/Cr-N main peak, without a discernible Fe-Fe/Cr-Cr peak, thus providing initial evidence for the atomic dispersion of the metal species. Further EXAFS fitting analyses (Figures S10C, D and Table S1) reveals that the coordination number of Fe-N/Cr-N in the first shell is approximately 4, indicating that Fe/Cr is coordinated with 4 N atoms; $CN_{Fe-Cr} = 0.5 \pm 0.2$ and $CN_{Cr-Fe} = 0.3 \pm 0.1$ in the second shells suggest the formation of weak interaction between Fe and Cr. Collectively, these findings demonstrate the structure of Cr=N_2=Fe ABCs illustrated in Figure 2C. The rigorous structure and morphology analysis above demonstrated that the pairs of heterometallic species were successfully anchored on the carbon substrate without aggregation.

The Cr 2p and Fe 2p spectra indicate that the oxidation state of Fe is closer to +2 (Figures 2G, S11A, and Table S2)[33,34], and that of Cr is +3 (Figures 2H and S12A).

XANES studies further demonstrate the valence state of the metal sites. The locations of Cr=N_2=Fe ABCs absorption edges indicate that the Fe and Cr atoms carry valence states of approximately +2 and +3, respectively (Figures S10A, B). In the C1s fine spectrum of XPS (Figure 2I), the fitting peak at 284.7 eV is attributed to sp^2 hybrid graphite carbon (C=C).[25,35] The smaller the full-width at half maxima (FWHM) of the conjugated C=C peak, the higher the π-electron delocalization degree.[35–37] As evidenced by the bar chart in Figure 2I, the FWHM of C=C in bimetals shows a significant shrink, undoubtedly increasing the delocalized electrons in the system. In addition, the N 1s spectra of Cr=N_2=Fe ABCs and control samples illustrates that the proportion of metal-N species in the SACs prepared by the Joule heating strategy is much higher than that in ZIF-8 derived SACs previously reported (Figures 2J, S11B, S12B, and Table S3).[2,16,38–40]

As an important supplement to XPS, ultraviolet photoelectron spectroscopy (UPS) is used to reflect the information of the associated band structure of the whole material (Figure 2K). Since the valence orbital is mainly involved in the combination with the oxygen intermediates, we firstly focused on the evaluation of the valence band energy levels (E_V) of the three catalysts. The valence band maximum (VBM) for Cr AMCs, Fe AMCs and Cr=N_2=Fe ABCs are estimated to be 3.72, 4.42 and 4.05 eV, respectively, indicating that the high occupied molecular orbital (HOMO) or E_V moved to the higher energy after the introduction of the heterometallic Cr in Fe AMCs (inset in Figure 2K). The increase of the HOMO (d_{z^2} orbital of metal) energy level will appropriately weaken its bonding ability with the intermediates, which is related to the pairing hardness (η_{DA}) between the donor and the acceptor that will be mentioned later.[25,41] The principle of "energy similarity" in bonding determines the ability of bonding, and the bond order reflects the strength of bonding. The binding between metal sites and intermediates should first depend on whether their orbital energy levels are close, and then on the size of the bond order. This is why there is a certain difference between the theoretical prediction (bond order: Cr>Fe) and the experimental data (bonding ability: Fe>Cr). The association of the three with the intermediates was also verified again in our subsequent in-situ experimental analysis. Secondly, when the bias voltage is applied on the UPS spectrum, the cutoff energy (E_{cutoff}) of Cr AMCs, Fe AMCs and Cr=N_2=Fe ABCs are 17.68, 17.42 and 17.29 eV, respectively. According to the work function (Ø) equation, Ø = 21.22 eV - E_{cutoff}, their Ø are 3.54, 3.80 and 3.93 eV, respectively. The smaller the Ø, the easier the electrons leave the metal. The electron density of the MN_4 moiety is

distributed more thinly at the metal center and more densely at the nitrogen ligand, inducing Fe 3*d* electron delocalization.[29] Different from the order of the size of E_v, the Ø value of Cr=N_2=Fe ABCs is larger than that of Fe AMCs, which may be related to the high delocalization degree (strong electron donor) of the carbon plane in Cr=N_2=Fe ABCs mentioned above. From this, the electron density of metal center in Cr=N_2=Fe ABCs is much larger than that in Fe AMCs, which is obviously beneficial for electron-donating processes during ORR. Cr=N_2=Fe ABCs with a moderate HOMO and a maximum Ø value may exhibit a proper association with the oxygen species, thus obtaining an excellent ORR catalytic capability. Two other UPS measurements are additionally provided to demonstrate that this trend of slight data differences is consistent (Figure S13).

3.3. The electrocatalytic ORR performance

The electrocatalytic ORR performance of Cr=N_2=Fe ABCs and related control samples was then evaluated in an O_2-saturated 0.1 M KOH electrolyte using a standard three-electrode system, with commercial Pt/C as a benchmark. Please note the supplementary note in Figure S14. All potentials here are presented versus the reversible hydrogen electrode (vs. RHE). As demonstrated by Figure 3A, the linear sweep voltammetry (LSV) curve of Cr=N_2=Fe ABCs shows an $E_{1/2}$ of 0.84 V and a limit current density (J_L) of 5.79 mA cm^{-2}, which is superior to the benchmark Pt/C ($E_{1/2}$ = 0.80 V and J_L = 5.24 mA cm^{-2}) and other controls including Fe AMCs ($E_{1/2}$ = 0.79 V and J_L = 4.61 mA cm^{-2}), Cr AMCs ($E_{1/2}$ = 0.73 V and J_L = 5.39 mA cm^{-2}) and NMCs ($E_{1/2}$ = 0.74 V and J_L = 3.98 mA cm^{-2}). The maximum diffusive J_L on the surface of Cr=N_2=Fe ABCs indicates an ORR process less controlled by the diffusion process, implying that the mass transfer process in the electrode reaction is easier, and the reactants diffused into the bilayer could be electrochemically reacted.[42] The intrinsic activity of SACs was classically evaluated by quantifying the turnover frequency (TOF) and mass activity (MA).[29,43] The TOF and MA values of Cr=N_2=Fe ABCs are significantly higher than those of Fe AMCs, Cr AMCs and Pt/C (Figure 3B), which intuitively illustrates the impact of the introduction of Cr on the intrinsic activity of the Fe site. Based on the above characterizations, we infer that the inherent activity improvement of Cr=N_2=Fe ABCs may be closely related to the following two points: (1) As shown in Figure 3F, the TOF value of Cr=N_2=Fe ABCs at 0.80 V is 6.51 e s^{-1} $site^{-1}$, which is about 3 times and 10 times higher than that of Fe AMCs (2.06 e s^{-1} $site^{-}$

^{1}) and Cr AMCs (0.65 e s^{-1} $site^{-1}$), respectively, indicating that the obvious increase of delocalized electrons can enhance the ORR catalytic ability of the material; (2) For this donor (*Fe)-acceptor (*OH) electron transfer reaction in the RDS of ORR, the ability of their interaction mainly depends on the energy gap (pairing hardness: η_{DA}) between Fe d_z^2 (HOMO) and *OH p_z+s orbitals (Figure 3G).[25,41] The smaller the η_{DA}, the stronger the interaction, and the more difficult it is to desorb *OH in RDS from the surface of the metal center. The above UPS characterization has proved that the HOMO (d_z^2 orbital of metal) energy level of Cr=N_2=Fe ABCs is moderate compared to those of single metal catalysts. Therefore, Cr=N_2=Fe ABCs have a proper binding with *OH in RDS, which is conducive to the ORR cycle.

The kinetic current density (J_k) of Cr=N_2=Fe ABCs calculated using the Koutecky-Levich equation[16] is far better than that of other prepared catalysts and Pt/C (Figure S15). An ultra-low Tafel value of 45.4 mV dec^{-1} is observed on Cr=N_2=Fe ABCs, which is lower than that of Pt/C (91.3 mV dec^{-1}), Fe AMCs (51.1 mV dec^{-1}) and Cr AMCs (56.7 mV dec^{-1}) (Figure 3C). Hence, the kinetic rate of forming oxygen intermediates on the surface of Cr=N_2=Fe ABCs is faster, and only less energy is required to complete the RDS of the ORR process on Cr=N_2=Fe ABCs.[44] To investigate the reaction selectivity of the prepared samples, the electron transfer number and H_2O_2 yield based on ring current and disk current were also calculated (Figure 3D). The calculated electron transfer number of Cr=N_2=Fe ABCs is close to 4.0 in the range of 0.1 to 0.8 V, manifesting that Cr=N_2=Fe ABCs catalyze the ORR process by a direct 4 e pathway with relatively low overpotential. In addition, the RRDE measurements also display that the H_2O_2 yield on Cr=N_2=Fe ABCs is less than 1 %, lower than that on Pt/C, elucidating that the release of peroxide (HO_2^-) during ORR is remarkably inhibited and that Cr=N_2=Fe ABCs are efficient in the direct reduction of O_2 to H_2O. The electrochemically active surface area (ECSA) is determined by measuring the double layer capacitance (C_{dl}) in the non-Faraday region to reflect the accessibility of the active sites in the electrocatalytic reaction (Figure S16, S17). In Figure S17, the ECSA of Cr=N_2=Fe ABCs, Fe AMCs and Cr AMCs, and commercial Pt/C are 562, 410, 652, and 407, respectively.

Long-term stability and methanol tolerance tests were performed on all the catalysts (Figure 3E). First, the long-term stability of the obtained catalysts was studied by voltammetry and chronoamperometry. After 5000 CV cycles (Figure S18), almost no obvious attenuation of $E_{1/2}$ is observed for Cr=N_2=Fe ABCs, compared with significant

negative excursions for Fe AMCs, Cr AMCs, and Pt/C (-10, -26, and -16 mV, respectively). The impressive stability of Cr=N_2=Fe ABCs was further verified by chronoamperometric measurements (Figure S19). After 40,000 s of continuous operation, the current retention rates of Cr=N_2=Fe ABCs and Cr AMCs are 90.7% and 94.6%, respectively, while the current retention rates of Fe AMCs and Pt/C decrease to 86.9% and 87.7%, respectively. Notably, the aberration-corrected HAADF-STEM image, EDS mapping and XRD patterns of Cr=N_2=Fe ABCs after chronoamperometry testing for 40,000 s displays that the metal atoms remain atomically dispersed on the carbon substrate, demonstrating the weak Fenton reactivity and excellent durability of Cr=N_2=Fe ABCs (Figure S20). Furthermore, no visible current oscillation is observed when adding 1.0 M methanol to Cr=N_2=Fe ABCs, whereas the current decreases markedly when adding methanol to Pt/C, signifying the excellent long-term tolerance of Cr=N_2=Fe ABCs to methanol (Figure S21). Overall, the results clearly support the major impact of the modulation of 3*d* valence orbital energy level on improving electrocatalytic ORR performance.

To further verify the potential of Cr=N_2=Fe ABCs to replace commercial Pt/C in real energy devices, self-assembled zinc-air batteries (ZABs) with Cr=N_2=Fe ABCs or Pt/C (20 %) as the air cathode and Zn foil as the anode were tested. The polarization and power density curves of the assembled ZABs are shown in Figure 3H. As expected, the Cr=N_2=Fe ABCs-driven ZAB exhibit a good peak power density of 147.6 mW cm^{-2}, which is superior to that of Pt/C-based ZAB (133.6 mW cm^{-2}). When normalized for Zn weight loss, the discharge specific capacity of ZAB assembled with Cr=N_2=Fe ABCs is 818.7 mAh g^{-1} at 10 mA cm^{-2}, which surpasses 694.6 mAh g^{-1} of the commercial Pt/C-based battery (Figures 3I and S22). Furthermore, as shown by the discharge curves at different current densities (Figure 3J), ZABs assembled with Cr=N_2=Fe ABCs maintain higher discharge voltages than their Pt/C-based counterparts, demonstrating excellent rate performance. Then Cr=N_2=Fe ABCs or Pt/C were coupled with the oxygen evolution catalyst RuO_2 (mass ratio = 1:1), and the constant current charge-discharge cycle life of the rechargeable ZABs assembled with them was examined separately. The Cr=N_2=Fe ABCs-based ZABs run continuously for more than 300 hours without significant changes in charge-discharge voltages, whereas the Pt/C-based ZAB shows an unstable increasing charge voltage and a decreasing discharge voltage (Figure 3K). The Cr=N_2=Fe ABCs cathode also feature a much lower charge/discharge voltage gap than that of Pt/C, narrowing to about 0.76 V. Together,

these electrochemical findings provide compelling evidence that Cr=N_2=Fe ABCs can serve as a competitive ORR catalyst, offering the potential to reduce or replace dependence on platinum-based catalysts (Table S4 and S5).

3.4. Valence electron behavior and bonding mechanisms

The oxygen electrocatalytic process involves spin-related electron transfer, making the reaction kinetics and thermodynamics sensitive to the electron configuration.[16,45] Therefore, based on the understanding of the metal valence orbital energy level, we further investigated 3d valence electron behavior and bonding mechanisms through the theoretical calculations and zero-field cooling (ZFC) temperature-dependent magnetic susceptibility measurements. According to the projected density of states (PDOS), the peak shapes of Cr=N_2=Fe ABCs compared to those of Fe AMCs and Cr AMCs undergone certain changes, indicating that the interaction between *d*-orbitals of the paired metal atoms triggers a certain degree of electronic reorganization (Figure 4A). Moreover, the total density of states (TDOS) demonstrates a structure-activity relationship that better electron-transfer activity for the ORR process can be achieved after the introduction of CrN_4 moieties (Figure S23). The differential charge density map (Figure 4B and S24-S26) and the Bader charge (Figure 4C) visually demonstrate the electronic modulation effect of Cr sites on Fe sites. After the introduction of the Cr site, the electron density at the Fe center significantly increases, while the electron density at the Cr center is lower than that in the Cr AMCs, indicating that the lower electronegativity of Cr (χ = 1.66) as an electron donor increases the electron density around the Fe (χ = 1.83). This increase in electron density not only benefits the moderate association of Fe centers to O,[22,46] but also shortens the bond length of Fe-N bonds, making a further important contribution to the stability of FeN_4 structure. The calculated electron density of different metal sites is in agreement with Ø obtained by UPS test.

To further quantify the 3*d* electron state of the metal sites, we calculated the unpaired electron number based on the results of the ZFC test, and the calculation details are in the Supporting Information. As demonstrated in Figure 4D, the calculated unpaired electron numbers of Fe AMCs and Cr AMCs are ~1.0 and ~1.2, respectively. According to the possible *d*-electron arrangements of Fe and Cr ions (Figure S27), it is evident that the metal sites in both monometallic materials obtained are in a low spin (LS) state. The unpaired electron number of Cr=N_2=Fe ABCs is ~5.3, indicating that more Pauli paramagnetic free electrons are formed within this material system after the coupling

of Fe and Cr. It can be deduced that the spin state of the metal sites in Cr=N_2=Fe ABCs increases to the medium spin (MS) state. Next, we focus on the effect of the spin state change at the metal site on the barrier of *OH dissociation (RDS for Cr=N_2=Fe ABCs and Fe AMCs). The orbital interactions between the metal sites with different spin states and *OH are illustrated in Figure 4E. It is worth noting that, according to the symmetry matching principle of bonding, the contribution of the interactions between the d_{xy} and $d_{x^2-y^2}$ orbitals of the metal ions and the ORR intermediate orbitals to bonding can be disregarded.[2] The bonding strength between the donor and the acceptor is quantified by calculating the bond order, assuming that the orbital energy levels of metal sites are consistent. (see Supporting Information for more calculation details). From a thermodynamic perspective, a smaller bond order for the product suggests a more favorable decrease in energy barrier for product release. The bond order of Fe (MS) in Cr=N_2=Fe ABCs to the product *OH of 1 is smaller than that of Fe (LS) in Fe AMCs to the product *OH of 1.5 (the top panel of Figure 4E), clearly demonstrating the thermodynamic advantage of product release and thus weakening the RDS energy barrier on the Fe site (the bottom panel of Figure 4E).

The variation in the bonding mechanisms with *OH is further confirmed by the change in the projected COHP (PCOHP) with different models. We mainly investigated the bonding/antibonding properties of the d_{z^2}-p, d_{yz}-p, and d_{xz}-p orbitals between the Cr=N_2=Fe ABCs, Fe AMCs and Cr AMCs with *OH (Figure 4F). The d_{z^2}-p_z antibonding orbital of the Fe AMCs is almost completely unoccupied, with all bonding and antibonding orbitals below the Fermi level fully occupied. However, the Cr=N_2=Fe ABCs (Fe) show fewer d_{z^2}-p, d_{yz}-p, and d_{xz}-p antibonding orbitals away from the Fermi level, suggesting fewer unoccupied antibonding orbitals that coincides with Figure 4E. Conversely, the antibonding orbitals of Cr=N_2=Fe ABCs (Cr) are much higher in energy than the Fermi level, indicating that Cr=N_2=Fe ABCs (Cr) has a stronger bond with *OH than Cr AMCs (consistent with Figure S28A). Of note, compared to Fe AMCs, Cr AMCs have fewer antibonding unoccupied orbitals and bonding orbitals, implying a lower adsorption of Cr AMCs for OH. Obviously, this result is inconsistent with the bond order (Fe: 1.5 < Cr: 2), but consistent with their valence orbital energy levels (Cr > Fe) (Figure 2K), which fully demonstrates the importance of prioritizing valence orbital energy levels. Moreover, in this fixed-energy level Cr=N_2=Fe ABCs system, the Cr site with a larger bond order of 2.5 for *OH can drive the local electrons flow from Fe to *OH to produce a bias towards O under the action of intermolecular van der Waals

forces or hydrogen bonds.[29] This accelerates the dissociation of *OH from the Fe site (bond order = 1) to regenerate active sites. In summary, the addition of heterogeneous metal Cr significantly alters the antibonding orbital occupancy and local electron bias of *OH at Fe sites, thereby reducing the binding strength or dissociation energy barrier between them.

3.5. In-situ FTIR and Raman analysis

To obtain the adsorption behaviors/mechanisms on the surface of Cr=N_2=Fe ABCs, in-situ attenuated total reflectance Fourier transform infrared (ATR-FTIR) spectroscopy was conducted (Figure 4G and 4H). The broad peak between 2769 and 2855 cm^{-1} is caused by the stretching vibration of O-H. The shift of OH peak reveals a weak interaction between metal center and OH, rather than a strong chemical bond.[44] As the potential shifts negatively, the IR peak for *v*(OH) of Cr=N_2=Fe ABCs gradually red-shift, indicating the weakened OH adsorption with the decreased overpotential. The weak peaks at 1135 and 1462 cm^{-1} correspond to $^*O_2^-$ and $^*O_2$, respectively.[47–49] As the negative shift of potential, the kinetics of ORR accelerate, bringing about the appearance and gradual increase of the $^*O_2^-$ peak while the intensity of $^*O_2$ gradually decreases. In contrast, a strong set of main peaks appears and intensifies significantly at 1243 and 1312 cm^{-1}, attributed to *OOH and M-OOH, respectively.[47,49,50] This phenomenon suggests that relative to $^*O_2^-$, the kinetic conversion rate of *OOH is faster. Furthermore, during ORR process, negligible changes in the position of M-OOH peak but significant variations in the intensity indicate a strong interaction between metal sites and *OOH.[44] The positive going feature near 1568 cm^{-1} in the IR spectra corresponds to bending vibrations of H-O-H in water, manifesting that H_2O molecules bind with intermediates on catalyst surfaces such as *OOH and $^*O_2^-$.[49]

Given that the characteristic peaks of metal-O bonds in the spectrum are generally below 1000 cm^{-1}, it is more necessary to further investigate the ORR process mechanism of the three catalysts using in-situ Raman spectroscopy to verify the rationality of the design in this study. In Figure 5, the peak near 415 cm^{-1} belongs to the inherent OH adsorption (*v*(M-OH)) on metal sites in alkaline solutions, which also validates the 3*d* orbital splitting mode of the metal sites (Figure S27); the small peak observed at about 377 cm^{-1} is attributed to *v*(Fe^{II}/Cr^{III}-OOH) of low valence metals, demonstrating the existence of Fenton effect.[50,51] The weaker above two peaks in bimetal can be attributed to the steric hindrance effect of its structure and lower H_2O_2

yield. The peaks around 679cm^{-1} and 642 cm^{-1} are primarily due to the adsorption of the generated high valence metals to OH (ν(Fe^{III}/Cr$^{N>III}$-OH)) and the formation of *OOH intermediates on active sites ν(Fe^{III}/Cr$^{N>III}$-OOH), respectively.[50,51] The intensity of the former group (377/415 cm^{-1}) decreases with decreasing applied potential, while that of the latter group (642/679 cm^{-1}) shows an opposite trend, indicating a conversion from Fe^{II} to Fe^{III} during the ORR process. The ν(Fe^{III}/Cr$^{N>III}$-OH) of Cr=N_2=Fe ABCs is much weaker than that of Fe AMCs, which is related to the increase of both orbital energy level and antibonding orbital occupancy on the one hand, and the weakening of Fe-OH bond on the other hand. It is worth mentioning that, compared to Fe AMCs and Cr AMCs, the ν(Fe^{III}/Cr$^{N>III}$-OH) in Cr=N_2=Fe ABCs with a significant red-shift indicates a weakening of the bond energy between the metal center and *OH,[49] which is conducive to the desorption of product *OH, and thus the promoted ORR activity. In Figure 5B, the strong Fenton reaction and the difficult *OH dissociation on the Fe sites in Fe AMCs give rise to a large accumulation of *OH on the catalyst surface,[17] forming a prominent ν(Fe^{III}-OH) peak. As the voltage decreases, it even exceeds the generated ν(Fe^{III}-OOH). Unlike the Fe sites, the weak Fenton reaction and high HOMO on Cr sites make ν(Cr$^{N>III}$-OH) much weaker than ν(Fe^{III}-OH) (Figure 5C).[19] Moreover, although the in-situ spectra show strong inherent adsorption of hydroxides in the electrolyte on both metal sites, the corrosion resistance of Cr sites remains stronger than that of Fe sites due to the solubility product constant of chromium hydroxide (Ksp = 6.3×10^{-31}) being much larger than that of iron hydroxide (Ksp = 4×10^{-38}). Such result is also evidenced by the stability of Fe AMCs poorer than Cr AMCs in chronoamperometry testing for 40,000 s (Figure 3E and Figure S19).

In Fe AMCs and Cr AMCs, the band at 576 cm^{-1} is assignable to Fe/Cr-O stretching caused by high oxygen coverage at the active sites (Figure 5B and 5C).[52] As reported by Nørskov et al., this stable adsorbed oxygen on the surface of the catalytic site will prevent electron and proton transfer at high potentials, leading to an ORR overpotential.[53] As the decreases in applied voltage, the M-$^{*}O_2$ peak at 576 cm^{-1} gradually diminishes, and the M-$^{*}O_2^{-}$ peak at 750 cm^{-1} progressively increases, implying that the first step in the ORR process is a single electron transfer ($^{*}O_2$+e^{-} →$^{*}O_2^{-}$). Meanwhile, the transformation between two oxygen species also establishes that the first electron transfer during oxygen electroreduction can be driven by an applied potential.[54] In addition, the peak near 1030 cm^{-1} comes from the O-O stretching vibration of OOH adsorbed on the active sites (Figure 5). Of note, the

*OOH/•OOH peak at Fe sites in Fe AMCs exhibits remarkable intensity, possibly indicating its pronounced initial reactivity towards ORR and strong Fenton effect (Figure 5B). However, owing to its stronger adsorption for the product *OH (~683 cm^{-1}) than *OOH (~641 cm^{-1}), the catalytic activity is reduced. For reactants, a higher peak intensity or bond energy indicates stronger reactivity because stable adsorption is required for reactants; but for products, easy desorption is needed, so peak intensity or bond energy should not be too strong. The peak around 1064 cm^{-1} is attributed to the bending mode of *OH/•OOH.[47,49] The above in-situ analysis results elucidate that the three catalysts have different kinetic mechanisms, which is consistent with the study of valence band and the theoretical calculation. These findings provide a basis for improving the catalytic activity of bimetallic systems.

4. Conclusion

In summary, we report a carbon-loaded Cr=N_2=Fe ABCs prepared by an advanced energy-saving Joule heating technique. The introduction of this metal center with low Fenton effect and *OH adsorption energy not only reduces the intrinsic Fenton reactivity of the material system, but also perturbs the valence band of the entire material, providing the possibility for improving catalytic activity and stability. Detailed valence band characterization and in-situ analysis reveal that the three resulting catalysts exhibits different kinetic mechanisms in the electrolyte. The improved performance can be attributed to the changes in the valence orbital level and antibonding orbital occupancy. The experimental data also demonstrate that the interaction between this donor (metal sites) and acceptor (oxygen species) depends first on the orbital level, and then can be further evaluated by the bond order. The bond order calculation without considering the orbital levels can lead to confusion for the explanation of catalytic mechanisms. This study provides positive inspiration for the preparation and regulation of highly efficient and stable non-precious metal electrocatalysts in energy conversion devices.

Declaration of competing interest

The authors declare that they have no known competing financial interests or personal relationships that could have appeared to influence the work reported in this paper.

Acknowledgements

The authors acknowledge the financial support provided by Major Science and Technology Projects of Yunnan Province (202302AB080019-3), the National Natural Science Foundation of China (52064049), Natural Science Foundation of Yunnan Province (202301AS070040), Key Laboratory of Solid-State Ions for Green Energy of Yunnan University, the Electron Microscope Center of Yunnan University and the authors would like to thank Shiyanjia Lab (www.shiyanjia.com) for the UPS test.

Appendix. Supplementary materials

Supplementary data associated with this article can be found in the online version.

Data availability

Data will be made available on request.

References

[1] R. Gao, J. Wang, Z.-F. Huang, R. Zhang, W. Wang, L. Pan, J. Zhang, W. Zhu, X. Zhang, C. Shi, J. Lim, J.-J. Zou, Pt/Fe_2O_3 with Pt–Fe pair sites as a catalyst for oxygen reduction with ultralow Pt loading, Nat. Energy. 6 (2021) 614–623. https://doi.org/10.1038/s41560-021-00826-5.

[2] L. Wang, Q. An, X. Sheng, Z. Mei, Q. Jing, X. Zhao, Q. Xu, L. Duan, X. Zou, H. Guo, Modulation of electronic spin state and construction of dual-atomic tandem reaction for enhanced pH-universal oxygen reduction, Appl. Catal. B Environ. 343 (2024) 123509. https://doi.org/10.1016/j.apcatb.2023.123509.

[3] X. Zhu, C. Hu, R. Amal, L. Dai, X. Lu, Heteroatom-doped carbon catalysts for zinc–air batteries: progress, mechanism, and opportunities, Energy Environ. Sci. 13 (2020) 4536–4563. https://doi.org/10.1039/D0EE02800B.

[4] F. Luo, A. Roy, M.T. Sougrati, A. Khan, D.A. Cullen, X. Wang, M. Primbs, A. Zitolo, F. Jaouen, P. Strasser, Structural and reactivity effects of secondary metal doping into iron-nitrogen-carbon catalysts for oxygen electroreduction, J. Am. Chem. Soc. 145 (2023) 14737–14747. https://doi.org/10.1021/jacs.3c03033.

[5] C. Chen, Y. Li, A. Huang, X. Liu, J. Li, Y. Zhang, Z. Chen, Z. Zhuang, Y. Wu, W.-C. Cheong, X. Tan, K. Sun, Z. Xu, D. Liu, Z. Wang, K. Zhou, C. Chen, Engineering molecular heterostructured catalyst for oxygen reduction reaction, J. Am. Chem. Soc. 145 (2023) 21273–21283. https://doi.org/10.1021/jacs.3c05371.

[6] F. Liu, L. Shi, X. Lin, B. Zhang, Y. Long, F. Ye, R. Yan, R. Cheng, C. Hu, D. Liu, J. Qiu, L. Dai, Fe/Co dual metal catalysts modulated by S-ligands for efficient acidic oxygen reduction in PEMFC, Sci. Adv. 9 (2024) eadg0366. https://doi.org/10.1126/sciadv.adg0366.

[7] Z. Sun, H. Zhang, L. Cao, X. Liu, D. Wu, X. Shen, X. Zhang, Z. Chen, S. Ru, X. Zhu, Z. Xia, Q. Luo, F. Xu, T. Yao, Understanding synergistic catalysis on Cu-Se dual atom sites via operando X-ray absorption spectroscopy in oxygen reduction reaction, Angew. Chemie Int. Ed. 62 (2023) e202217719. https://doi.org/10.1002/anie.202217719.

[8] Z. Pei, H. Zhang, Y. Guo, D. Luan, X. Gu, X.W. (David) Lou, Atomically dispersed Fe sites regulated by adjacent single Co atoms anchored on N-P Co-doped carbon structures for highly efficient oxygen reduction reaction, Adv. Mater. 36 (2023) 2306047. https://doi.org/10.1002/adma.202306047.

[9] D.X. Luong, K. V Bets, W.A. Algozeeb, M.G. Stanford, C. Kittrell, W. Chen, R. V Salvatierra, M. Ren, E.A. McHugh, P.A. Advincula, Z. Wang, M. Bhatt, H. Guo, V. Mancevski, R. Shahsavari, B.I. Yakobson, J.M. Tour, Gram-scale bottom-up flash graphene synthesis, Nature. 577 (2020) 647–651. https://doi.org/10.1038/s41586-020-1938-0.

[10] Y. Yao, Z. Huang, P. Xie, S.D. Lacey, R.J. Jacob, H. Xie, F. Chen, A. Nie, T. Pu, M. Rehwoldt, D. Yu, M.R. Zachariah, C. Wang, R. Shahbazian-Yassar, J. Li, L. Hu, Carbothermal shock synthesis of high-entropy-alloy nanoparticles, Science. 359 (2018) 1489–1494. https://doi.org/10.1126/science.aan5412.

[11] J. Tian, R. Kong, Z. Wang, L. Fang, T. He, D. Jiang, H. Peng, T. Sun, Y. Zhu, Y. Wang, Enhancing methane combustion activity by modulating the local

environment of Pd single atoms in Pd_1/CeO_2 catalysts, ACS Catal. 14 (2024) 183–191. https://doi.org/10.1021/acscatal.3c02167.

[12] D. Xi, J. Li, J. Low, K. Mao, R. Long, J. Li, Z. Dai, T. Shao, Y. Zhong, Y. Li, Z. Li, X.J. Loh, L. Song, E. Ye, Y. Xiong, Limiting the uncoordinated N species in M–N single-atom catalysts toward electrocatalytic CO_2 reduction in broad voltage range, Adv. Mater. 34 (2022) 2104090. https://doi.org/10.1002/adma.202104090.

[13] Y. Yao, Z. Huang, P. Xie, L. Wu, L. Ma, T. Li, Z. Pang, M. Jiao, Z. Liang, J. Gao, Y. He, D.J. Kline, M.R. Zachariah, C. Wang, J. Lu, T. Wu, T. Li, C. Wang, R. Shahbazian-Yassar, L. Hu, High temperature shockwave stabilized single atoms, Nat. Nanotechnol. 14 (2019) 851–857. https://doi.org/10.1038/s41565-019-0518-7.

[14] A. Zitolo, V. Goellner, V. Armel, M.-T. Sougrati, T. Mineva, L. Stievano, E. Fonda, F. Jaouen, Identification of catalytic sites for oxygen reduction in iron- and nitrogen-doped graphene materials, Nat. Mater. 14 (2015) 937–942. https://doi.org/10.1038/nmat4367.

[15] N. Zhang, T. Zhou, M. Chen, H. Feng, R. Yuan, C. Zhong, W. Yan, Y. Tian, X. Wu, W. Chu, C. Wu, Y. Xie, High-purity pyrrole-type FeN_4 sites as a superior oxygen reduction electrocatalyst, Energy Environ. Sci. 13 (2020) 111–118. https://doi.org/10.1039/C9EE03027A.

[16] L. Wang, Z. Mei, Q. An, X. Sheng, Q. Jing, W. Huang, X. Wang, X. Zou, H. Guo, Modulating the electronic spin state of atomically dispersed iron sites by adjacent zinc atoms for enhanced spin-dependent oxygen electrocatalysis, Chem Catal. 3 (2023) 100758. https://doi.org/10.1016/j.checat.2023.100758.

[17] Y. Chen, R. Gao, S. Ji, H. Li, K. Tang, P. Jiang, H. Hu, Z. Zhang, H. Hao, Q. Qu, X. Liang, W. Chen, J. Dong, D. Wang, Y. Li, Atomic-level modulation of electronic density at cobalt single-atom sites derived from metal–organic frameworks: enhanced oxygen reduction performance, Angew. Chemie Int. Ed. 60 (2021) 3212–3221. https://doi.org/10.1002/anie.202012798.

[18] L.-N. Chen, W.-S. Yu, T. Wang, X.-D. Yang, H.-J. Yang, Z.-X. Chen, T. Wang, N. Tian, Z.-Y. Zhou, S.-G. Sun, Fluorescence detection of hydroxyl radical generated from oxygen reduction on Fe/N/C catalyst, Sci. China Chem. 63 (2020) 198–202. https://doi.org/10.1007/s11426-019-9635-2.

[19] E. Luo, H. Zhang, X. Wang, L. Gao, L. Gong, T. Zhao, Z. Jin, J. Ge, Z. Jiang, C. Liu, W. Xing, Single-atom Cr−N_4 sites designed for durable oxygen reduction catalysis in acid media, Angew. Chemie Int. Ed. 58 (2019) 12469–12475. https://doi.org/10.1002/anie.201906289.

[20] L. Zeng, Z. Zhao, Q. Huang, C. Zhou, W. Chen, K. Wang, M. Li, F. Lin, H. Luo, Y. Gu, L. Li, S. Zhang, F. Lv, G. Lu, M. Luo, S. Guo, Single-atom Cr–N_4 sites with high oxophilicity interfaced with Pt atomic clusters for practical alkaline hydrogen evolution catalysis, J. Am. Chem. Soc. 145 (2023) 21432–21441. https://doi.org/10.1021/jacs.3c06863.

[21] Y. Zuo, S. Bellani, G. Saleh, M. Ferri, D. V Shinde, M.I. Zappia, J. Buha, R. Brescia, M. Prato, R. Pascazio, A. Annamalai, D.O. de Souza, L. De Trizio, I. Infante, F. Bonaccorso, L. Manna, Ru–Cu nanoheterostructures for efficient hydrogen evolution reaction in alkaline water electrolyzers, J. Am. Chem. Soc. 145 (2023) 21419–21431. https://doi.org/10.1021/jacs.3c06726.

[22] X. Wei, S. Song, W. Cai, X. Luo, L. Jiao, Q. Fang, X. Wang, N. Wu, Z. Luo, H. Wang, Z. Zhu, J. Li, L. Zheng, W. Gu, W. Song, S. Guo, C. Zhu, Tuning the spin state of Fe single atoms by Pd nanoclusters enables robust oxygen reduction with dissociative pathway, Chem. 9 (2023) 181–197. https://doi.org/10.1016/j.chempr.2022.10.001.

[23] Y. Dai, B. Liu, Z. Zhang, P. Guo, C. Liu, Y. Zhang, L. Zhao, Z. Wang, Tailoring the d-orbital splitting manner of single atomic sites for enhanced oxygen reduction, Adv. Mater. 35 (2023) 2210757. https://doi.org/10.1002/adma.202210757.

[24] Y. Chen, S. Ji, Y. Wang, J. Dong, W. Chen, Z. Li, R. Shen, L. Zheng, Z. Zhuang, D. Wang, Y. Li, Isolated single iron atoms anchored on N-doped porous carbon

as an efficient electrocatalyst for the oxygen reduction reaction, Angew. Chemie Int. Ed. 56 (2017) 6937–6941. https://doi.org/10.1002/anie.201702473.

[25] N. Ramaswamy, U. Tylus, Q. Jia, S. Mukerjee, Activity descriptor identification for oxygen reduction on nonprecious electrocatalysts: Linking surface science to coordination chemistry, J. Am. Chem. Soc. 135 (2013) 15443–15449. https://doi.org/10.1021/ja405149m.

[26] Z. Shi, W. Yang, Y. Gu, T. Liao, Z. Sun, Metal-nitrogen-doped carbon materials as highly efficient catalysts: Progress and rational design, Adv. Sci. 7 (2020) 2001069. https://doi.org/10.1002/advs.202001069.

[27] G. Yang, J. Zhu, P. Yuan, Y. Hu, G. Qu, B.-A. Lu, X. Xue, H. Yin, W. Cheng, J. Cheng, W. Xu, J. Li, J. Hu, S. Mu, J.-N. Zhang, Regulating Fe-spin state by atomically dispersed Mn-N in Fe-N-C catalysts with high oxygen reduction activity, Nat. Commun. 12 (2021) 1734. https://doi.org/10.1038/s41467-021-21919-5.

[28] T. Ouyang, X.-T. Wang, X.-Q. Mai, A.-N. Chen, Z.-Y. Tang, Z.-Q. Liu, Coupling magnetic single-crystal $Co_2Mo_3O_8$ with ultrathin nitrogen-rich carbon layer for oxygen evolution reaction, Angew. Chemie Int. Ed. 59 (2020) 11948–11957. https://doi.org/10.1002/anie.202004533.

[29] Z. Li, Z. Zhuang, F. Lv, H. Zhu, L. Zhou, M. Luo, J. Zhu, Z. Lang, S. Feng, W. Chen, L. Mai, S. Guo, The marriage of the FeN_4 moiety and MXene boosts oxygen reduction catalysis: Fe 3d electron delocalization matters, Adv. Mater. 30 (2018) 1803220. https://doi.org/10.1002/adma.201803220.

[30] F. Yu, C. Jia, X. Wu, L. Sun, Z. Shi, T. Teng, L. Lin, Z. He, J. Gao, S. Zhang, L. Wang, S. Wang, X. Zhu, Rapid self-heating synthesis of Fe-based nanomaterial catalyst for advanced oxidation, Nat. Commun. 14 (2023) 4975. https://doi.org/10.1038/s41467-023-40691-2.

[31] H. Li, S. Di, P. Niu, S. Wang, J. Wang, L. Li, A durable half-metallic diatomic catalyst for efficient oxygen reduction, Energy Environ. Sci. 15 (2022) 1601–1610. https://doi.org/10.1039/D1EE03194E.

[32] T. He, Y. Chen, Q. Liu, B. Lu, X. Song, H. Liu, M. Liu, Y.-N. Liu, Y. Zhang, X. Ouyang, S. Chen, Theory-guided regulation of FeN_4 spin state by neighboring Cu atoms for enhanced oxygen reduction electrocatalysis in flexible metal–air batteries, Angew. Chemie Int. Ed. 61 (2022) e202201007. https://doi.org/10.1002/anie.202201007.

[33] T. Li, Y. Hu, K. Liu, J. Yin, Y. Li, G. Fu, Y. Zhang, Y. Tang, Hollow yolk-shell nanoboxes assembled by Fe-doped Mn_3O_4 nanosheets for high-efficiency electrocatalytic oxygen reduction in Zn-Air battery, Chem. Eng. J. 427 (2022) 131992. https://doi.org/10.1016/j.cej.2021.131992.

[34] Z. Li, X. Wu, X. Jiang, B. Shen, Z. Teng, D. Sun, G. Fu, Y. Tang, Surface carbon layer controllable Ni_3Fe particles confined in hierarchical N-doped carbon framework boosting oxygen evolution reaction, Adv. Powder Mater. 1 (2022) 100020. https://doi.org/https://doi.org/10.1016/j.apmate.2021.11.007.

[35] H. Darmstadt, C. Roy, Surface spectroscopic study of basic sites on carbon blacks, Carbon. 41 (2003) 2662–2665. https://doi.org/10.1016/S0008-6223(03)00325-7.

[36] S. Maldonado, S. Morin, K.J. Stevenson, Structure, composition, and chemical reactivity of carbon nanotubes by selective nitrogen doping, Carbon. 44 (2006) 1429–1437. https://doi.org/10.1016/j.carbon.2005.11.027.

[37] T. Takahagi, A. Ishitani, XPS study on the surface structure of carbon fibers using chemical modification and C1s line shape analysis, Carbon. 26 (1988) 389–395. https://doi.org/10.1016/0008-6223(88)90231-X.

[38] Z. Li, Y. Chen, S. Ji, Y. Tang, W. Chen, A. Li, J. Zhao, Y. Xiong, Y. Wu, Y. Gong, T. Yao, W. Liu, L. Zheng, J. Dong, Y. Wang, Z. Zhuang, W. Xing, C.T. He, C. Peng, W.C. Cheong, Q. Li, M. Zhang, Z. Chen, N. Fu, X. Gao, W. Zhu, J. Wan, J. Zhang, L. Gu, S. Wei, P. Hu, J. Luo, J. Li, C. Chen, Q. Peng, X. Duan, Y. Huang, X.M. Chen, D. Wang, Y. Li, Iridium single-atom catalyst on nitrogen-doped carbon for formic acid oxidation synthesized using a general host–guest strategy, Nat. Chem. 12 (2020) 764–772. https://doi.org/10.1038/s41557-020-

0473-9.

[39] Y. Zhan, T. Zhao, X. Wu, X. Gao, R. Huang, Z. Zhang, P. Li, X. Guan, C. Chen, X. Liu, X. Tang, N. Wang, H. Meng, Strengthening the oxygen reduction stability and activity of single iron active sites via a simultaneously electronic regulation and structure design strategy, Appl. Catal. B Environ. Energy. 357 (2024) 124254. https://doi.org/10.1016/j.apcatb.2024.124254.

[40] L. Zhao, J. Yu, C. Xing, Z. Ullah, C. Yu, S. Zhu, M. Chen, W. Li, Q. Li, L. Liu, Nanopore confined anthraquinone in MOF-derived N-doped microporous carbon as stable organic cathode for lithium-ion battery, Energy Storage Mater. 22 (2019) 433–440. https://doi.org/10.1016/j.ensm.2019.02.003.

[41] G.I. Cárdenas-Jirón, J.H. Zagal, Donor–acceptor intermolecular hardness on charge transfer reactions of substituted cobalt phthalocyanines, J. Electroanal. Chem. 497 (2001) 55–60. https://doi.org/10.1016/S0022-0728(00)00434-4.

[42] Q. Li, D. Zhang, J. Wu, S. Dai, H. Liu, M. Lu, R. Cui, W. Liang, D. Wang, P. Xi, M. Liu, H. Li, L. Huang, Cation-deficient perovskites greatly enhance the electrocatalytic activity for oxygen reduction reaction, Adv. Mater. 36 (2024) 2309266. https://doi.org/10.1002/adma.202309266.

[43] E. Zhu, T. Zheng, J. Yu, C. Shi, L. Zhou, H. Jin, J. Yang, G. Luo, D. Wei, X. Yang, M. Xu, Electron redistribution and proton transfer induced by atomically fully exposed Cu-O-Fe clusters coupled with single-atom sites for efficient oxygen electrocatalysis, Energy Storage Mater. 69 (2024) 103410. https://doi.org/https://doi.org/10.1016/j.ensm.2024.103410.

[44] L.-J. Yuan, B. Liu, L. Shen, Y.-K. Dai, Q. Li, C. Liu, W. Gong, X.-L. Sui, Z.-B. Wang, d-orbital electron delocalization realized by axial Fe_4C atomic clusters delivers high-performance Fe–N–C catalysts for oxygen reduction reaction, Adv. Mater. 35 (2023) 2305945. https://doi.org/10.1002/adma.202305945.

[45] Y. Sun, S. Sun, H. Yang, S. Xi, J. Gracia, Z.J. Xu, Spin-related electron transfer and orbital interactions in oxygen electrocatalysis, Adv. Mater. 32 (2020) 2003297. https://doi.org/10.1002/adma.202003297.

[46] X. Guo, J. Gu, S. Lin, S. Zhang, Z. Chen, S. Huang, Tackling the Activity and Selectivity Challenges of Electrocatalysts toward the Nitrogen Reduction Reaction via Atomically Dispersed Biatom Catalysts, J. Am. Chem. Soc. 142 (2020) 5709–5721. https://doi.org/10.1021/jacs.9b13349.

[47] M. Li, H. Zhu, Q. Yuan, T. Li, M. Wang, P. Zhang, Y. Zhao, D. Qin, W. Guo, B. Liu, X. Yang, Y. Liu, Y. Pan, Proximity electronic effect of Ni/Co diatomic sites for synergistic promotion of electrocatalytic oxygen reduction and hydrogen evolution, Adv. Funct. Mater. 33 (2023) 2210867. https://doi.org/10.1002/adfm.202210867.

[48] S. Huang, D. Tranca, F. Rodríguez-Hernández, J. Zhang, C. Lu, J. Zhu, H.-W. Liang, X. Zhuang, Well-defined N_3C_1-anchored single-metal-sites for oxygen reduction reaction, Angew. Chemie Int. Ed. 63 (2024) e202314833. https://doi.org/10.1002/anie.202314833.

[49] Y. Zhao, H.-C. Chen, X. Ma, J. Li, Q. Yuan, P. Zhang, M. Wang, J. Li, M. Li, S. Wang, H. Guo, R. Hu, K.-H. Tu, W. Zhu, X. Li, X. Yang, Y. Pan, Vacancy defects inductive effect of asymmetrically coordinated single-atom Fe-N_3S_1 active sites for robust electrocatalytic oxygen reduction with high turnover frequency and mass activity, Adv. Mater. 36 (2024) 2308243. https://doi.org/10.1002/adma.202308243.

[50] Y. Wang, P. Meng, Z. Yang, M. Jiang, J. Yang, H. Li, J. Zhang, B. Sun, C. Fu, Regulation of atomic Fe-spin state by crystal field and magnetic field for enhanced oxygen electrocatalysis in rechargeable zinc-air batteries, Angew. Chemie Int. Ed. 62 (2023) e202304229. https://doi.org/10.1002/anie.202304229.

[51] H. Zhong, K.H. Ly, M. Wang, Y. Krupskaya, X. Han, J. Zhang, J. Zhang, V. Kataev, B. Büchner, I.M. Weidinger, S. Kaskel, P. Liu, M. Chen, R. Dong, X. Feng, A phthalocyanine-based layered two-dimensional conjugated metal-organic framework as a highly efficient electrocatalyst for the oxygen reduction reaction, Angew. Chemie Int. Ed. 58 (2019) 10677–10682. https://doi.org/10.1002/anie.201907002.

[52] Y.-H. Wang, J.-B. Le, W.-Q. Li, J. Wei, P.M. Radjenovic, H. Zhang, X.-S. Zhou, J. Cheng, Z.-Q. Tian, J.-F. Li, In situ spectroscopic insight into the origin of the enhanced performance of bimetallic nanocatalysts towards the oxygen reduction reaction (ORR), Angew. Chemie Int. Ed. 58 (2019) 16062–16066. https://doi.org/10.1002/anie.201908907.

[53] J.K. Nørskov, J. Rossmeisl, A. Logadottir, L. Lindqvist, J.R. Kitchin, T. Bligaard, H. Jónsson, Origin of the overpotential for oxygen reduction at a fuel-cell cathode, J. Phys. Chem. B. 108 (2004) 17886–17892. https://doi.org/10.1021/jp047349j.

[54] G. Ye, S. Liu, K. Zhao, Z. He, Singlet oxygen induced site-specific etching boosts nitrogen-carbon sites for high-efficiency oxygen reduction, Angew. Chemie Int. Ed. 62 (2023) e202303409. https://doi.org/https://doi.org/10.1002/anie.202303409.

Figures and Captions

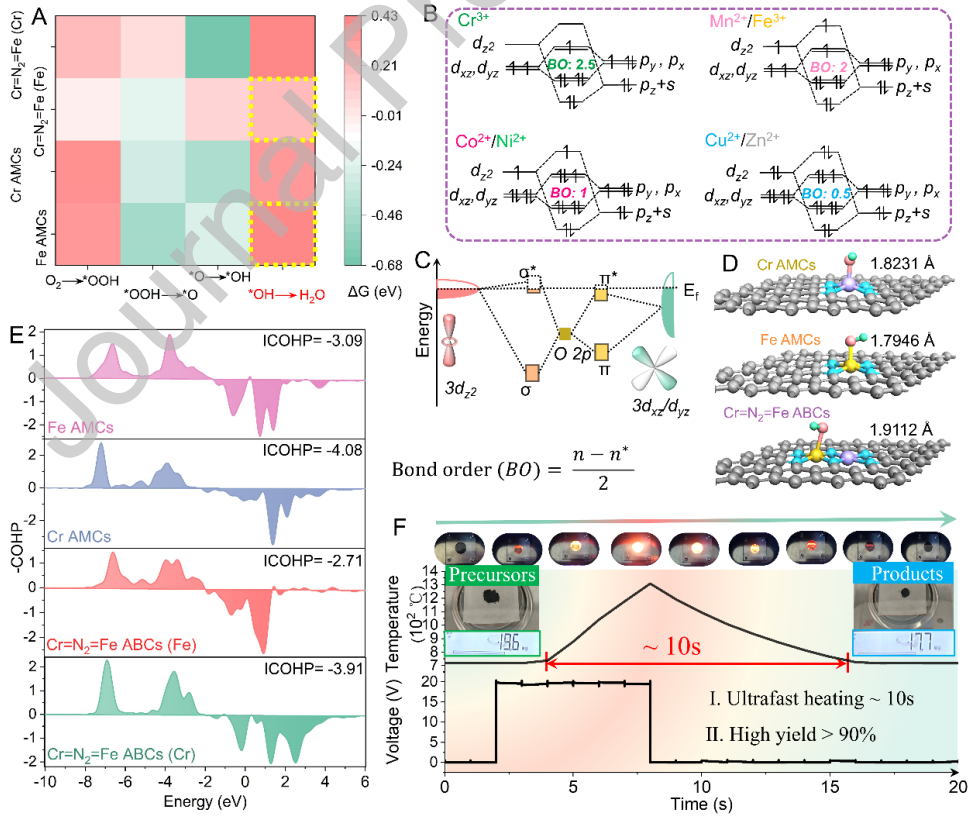

Figure 1. (A) ORR free-energy mapping at 1.23 V for the three models and the corresponding ORR mechanisms of the optimal Cr=N_2=Fe ABCs. (B) The bond order

between several transition metal ions with ORR potential and intermediate *OH. (C) Illustration of orbital interactions between metal sites (d_z^2, d_{xz} and d_{yz}) and adsorbed *OH ($2p$). (D) The length of metal-O with *OH adsorbed on the three models. (E) Crystal orbital Hamilton population (COHP) analysis and the integral COHP (ICOHP) value of *OH absorbed on the corresponding metal sites. (F) Temperature and voltage evolution during joule heating (bottom) and optical images before, during, and after heating of the precursors in the Joule furnace (top).

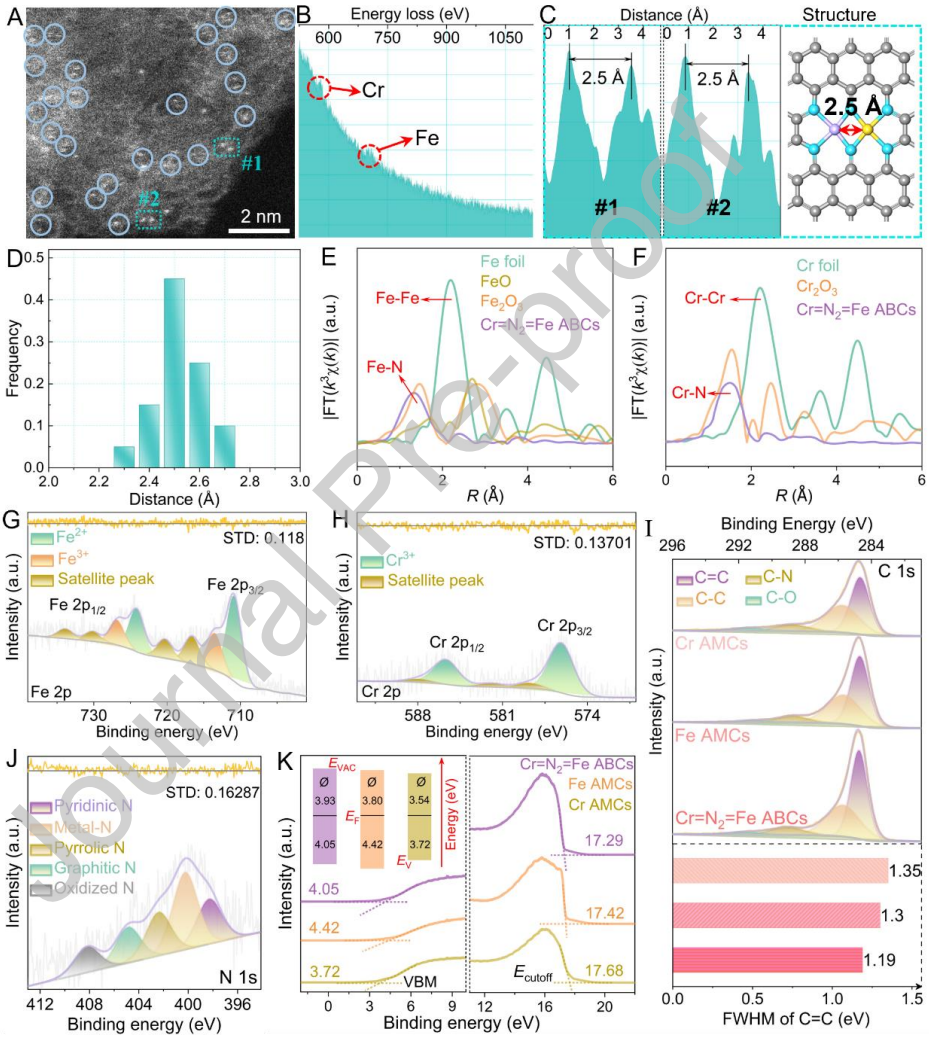

Figure 2. (A) Aberration-corrected HAADF-STEM image and (B) EELS of Cr=N_2=Fe ABCs. (C) The intensity profiles obtained on two bimetallic sites and the corresponding theoretical model. (D) Statistical Cr-Fe distance in the observed diatomic pairs. The k^3-weighted (E) Fe K-edge and (F) Cr K-edge Fourier-transform EXAFS spectra of Cr=N_2=Fe ABCs and references. High-resolution (G)Fe 2p and (H) Cr 2p XPS spectra of Cr=N_2=Fe ABCs. (I) The C1s XPS spectra and the corresponding full-width at half

maxima (FWHM) of C=C peak for the as-prepared electrocatalysts. (J) High-resolution N 1s XPS spectra of Cr=N_2=Fe ABCs. (K) The UPS spectra of Cr=N_2=Fe ABCs, Fe AMCs, and Cr AMCs.

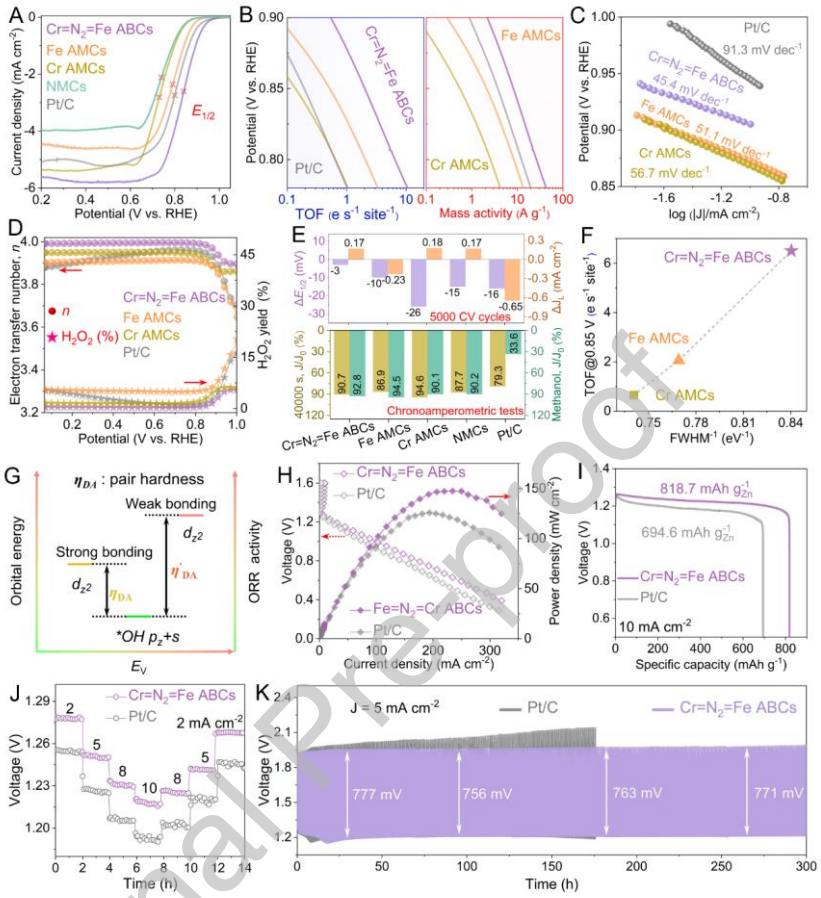

Figure 3. (A) LSV polarization curves, (B) turnover frequency and mass activity, (C) Tafel plots, (D) the electron transfer number and H_2O_2 yield, (E) comparison of stability of Cr=N_2=Fe ABCs, Fe AMCs, Cr AMCs and Pt/C in O_2-saturated 0.1 M KOH solution. (F) The relationship between catalytic activity (quantified by TOF) and π-electron delocalization degree (quantified by $FWHM^{-1}$). (G) The pairing hardness (η_{DA}) between the donor (*Fe or *Cr) on the catalysts and the acceptor (*OH). (H) Polarization and power density, (I) specific capacities, (J) galvanostatic discharge with different current densities, and (K) galvanostatic discharge-charge cycling of ZABs driven by both Cr=N_2=Fe ABCs and the benchmark Pt/C.

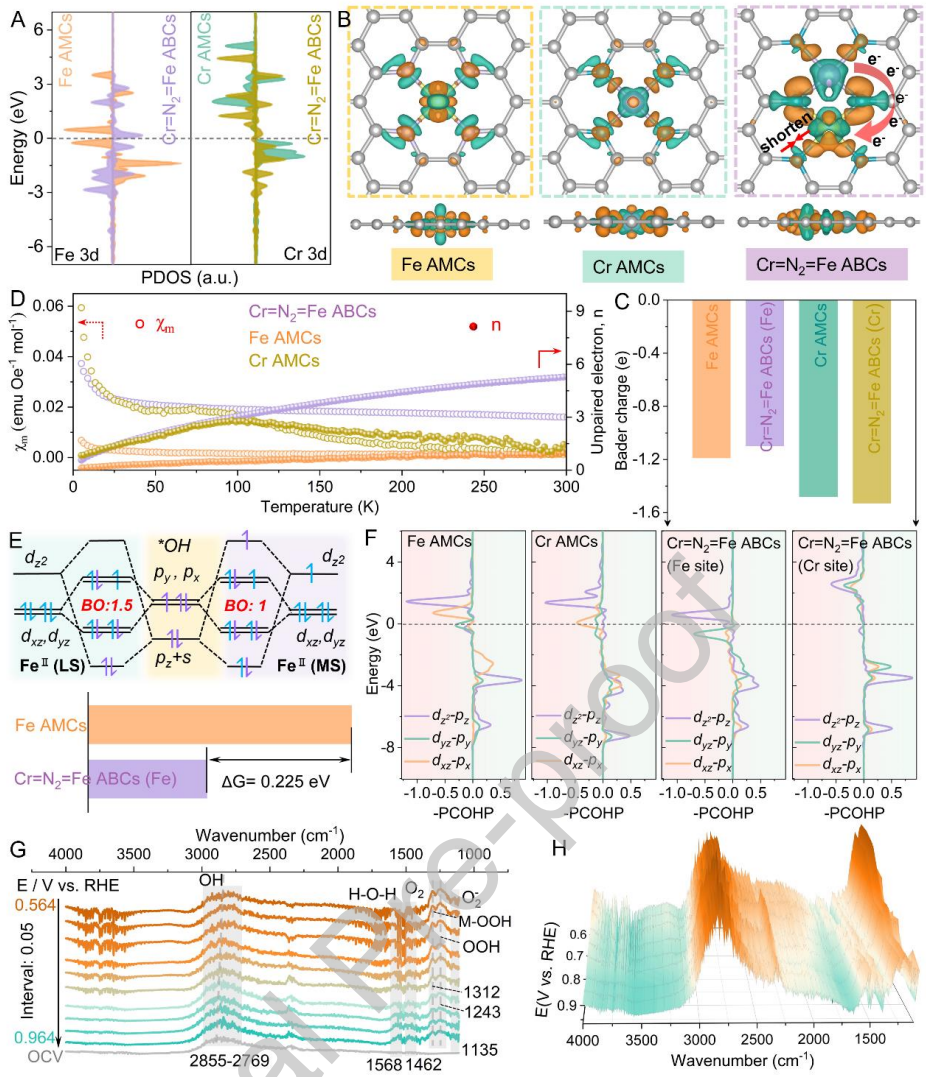

Figure 4. (A) The projected density of states (PDOS) for the total iron/chromium *d* orbital. (B) Top and side views of 3D differential charge density (cyan and orange represent charge depletion and accumulation, respectively). (C) Bader charge transfers at Fe and Cr sites in corresponding structural models. (D) χ_m and unpaired valence electron plots of all metal-containing samples. (E) The orbital interactions between Fe sites and the RDS intermediates (top), and the bar chart of the change in Gibbs free energy of RDS (bottom). (F) The PCOHP analysis of absorbed *OH onto Fe and Cr sites. (G) 2D in-situ ATR-FTIR spectra and (H) 3D in-situ ATR-FTIR spectra for Cr=N_2=Fe ABCs at different potentials in O_2-saturated 0.1 M KOH.

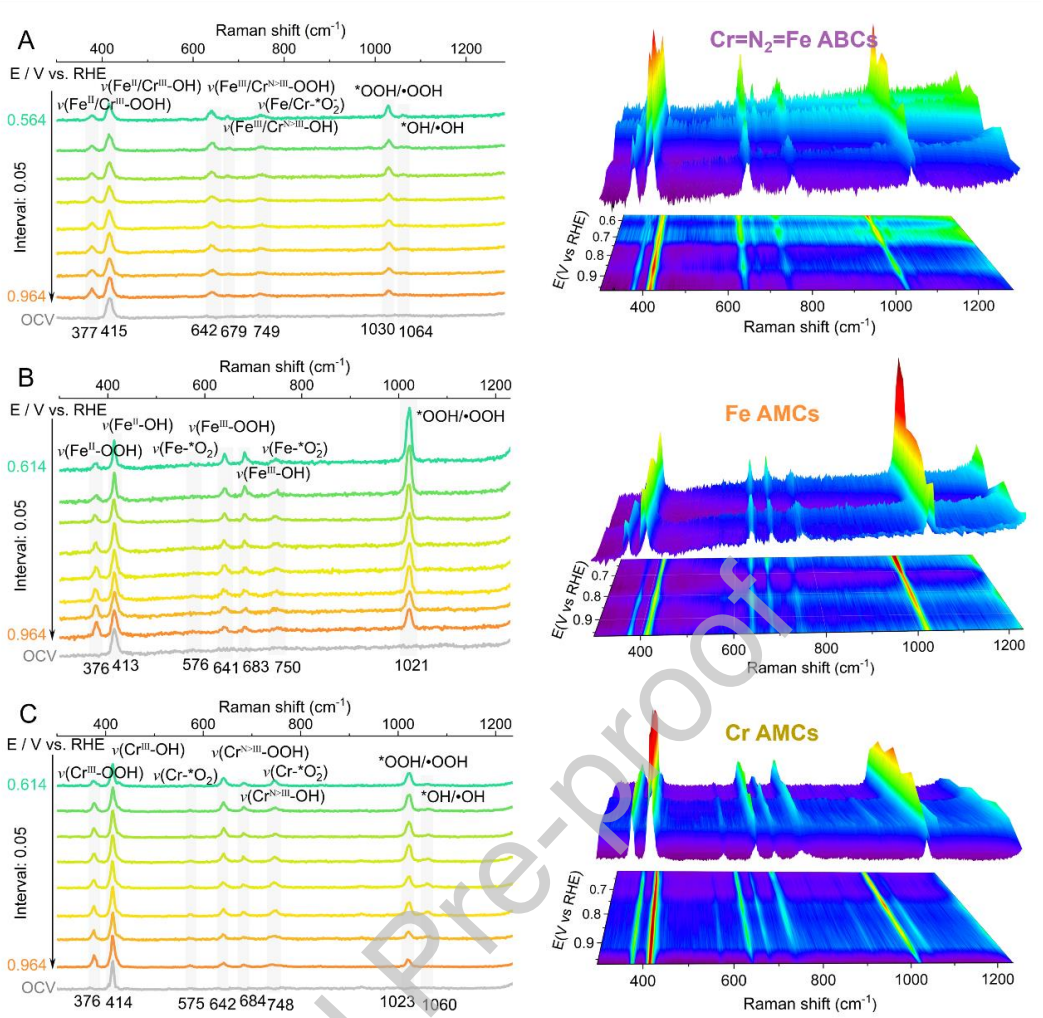

Figure 5. 2D in-situ Raman spectra and corresponding 3D in-situ Raman spectra of (A) Cr=N_2=Fe ABCs, (B) Fe AMCs, and (C) Cr AMCs during the ORR process in 0.1 M KOH.

Graphical Abstract

This study found that the interaction between metal sites and oxygen intermediates mainly depends on orbital energy levels before being further evaluated by bond order involving electronic regulation. The introduction of the Cr centers perturbs the valence band of the entire material, providing the possibility for improving ORR activity.

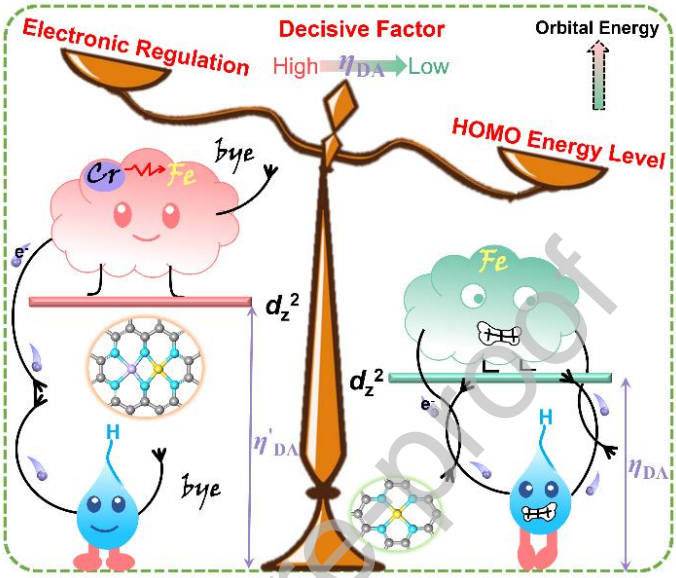

Declaration of interests

☒ The authors declare that they have no known competing financial interests or personal relationships that could have appeared to influence the work reported in this paper.

☐ The authors declare the following financial interests/personal relationships which may be considered as potential competing interests: